L-Edge X-ray Absorption Spectroscopy and DFT Calculations on Cu₂O₂ Species: Direct Electrophilic Aromatic Attack by Side-on Peroxo Bridged Dicopper(II) Complexes

Munzarin F. Qayyum,[†] Ritimukta Sarangi,[‡] Kiyoshi Fujisawa,[§] T. Daniel P. Stack,[†] Kenneth D. Karlin,[‖] Keith O. Hodgson,*,[†,‡] Britt Hedman,*,[‡] and Edward I. Solomon*,[†,‡]

[†]Department of Chemistry, Stanford University, Stanford, California 94305, United States

[‡]Stanford Synchrotron Radiation Lightsource, SLAC, Stanford University, Menlo Park, California 94025, United States

[§]Department of Chemistry, College of Sciences, Ibaraki University, 2-1-1 Bunkyo, Mito, Ibaraki 310-8512, Japan

[‖]Department of Chemistry, The Johns Hopkins University, Baltimore, Maryland 21218, United States

S *Supporting Information*

ABSTRACT: The hydroxylation of aromatic substrates catalyzed by coupled binuclear copper enzymes has been observed with side-on-peroxo-dicopper(II) (**P**) and bis-μ-oxo-dicopper(III) (**O**) model complexes. The substrate-bound-**O** intermediate in $[Cu(II)_2(DBED)_2(O)_2]^{2+}$ (DBED = N,N'-di-*tert*-butyl-ethylenediamine) was shown to perform aromatic hydroxylation. For the $[Cu(II)_2(NO_2\text{-}XYL)(O_2)]^{2+}$ complex, only a **P** species was spectroscopically observed. However, it was not clear whether this O−O bond cleaves to proceed through an **O**-type structure along the reaction coordinate for

hydroxylation of the aromatic xylyl linker. Accurate evaluation of these reaction coordinates requires reasonable quantitative descriptions of the electronic structures of the **P** and **O** species. We have performed Cu L-edge XAS on two well-characterized **P** and **O** species to experimentally quantify the Cu 3d character in their ground state wave functions. The lower per-hole Cu character ($40 \pm 6\%$) corresponding to higher covalency in the **O** species compared to the **P** species ($52 \pm 4\%$) reflects a stronger bonding interaction of the bis-μ-oxo core with the Cu(III) centers. DFT calculations show that 10−20% Hartree−Fock (HF) mixing for **P** and ~38% for **O** species are required to reproduce the Cu−O bonding; for the **P** species this HF mixing is also required for an antiferromagnetically coupled description of the two Cu(II) centers. B3LYP (with 20% HF) was, therefore, used to calculate the hydroxylation reaction coordinate of **P** in $[Cu(II)_2(NO_2\text{-}XYL)(O_2)]^{2+}$. These experimentally calibrated calculations indicate that the electrophilic attack on the aromatic ring does not involve formation of a $Cu(III)_2(O^{2-})_2$ species. Rather, there is direct electron donation from the aromatic ring into the peroxo σ^* orbital of the $Cu(II)_2(O_2^{2-})$ species, leading to concerted C−O bond formation with O−O bond cleavage. Thus, species **P** is capable of direct hydroxylation of aromatic substrates without the intermediacy of an **O**-type species.
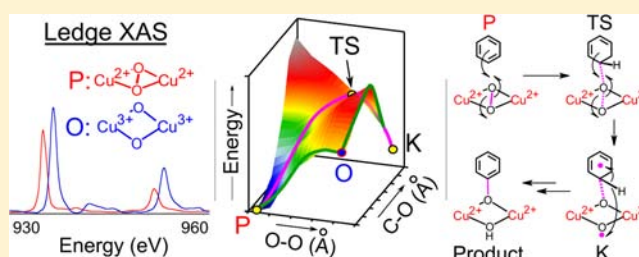
1. INTRODUCTION

The coupled binuclear copper (CBC) proteins bind molecular oxygen (O_2) to form a side-on μ-η^2:η^2 peroxo dicopper(II) species (**P**) (Scheme 1, top).[1−6] The CBC proteins include hemocyanin (Hc), catechol oxidase (CO), tyrosinase (Ty), and NspF and are involved in a range of biological functions. Hemocyanin is the dioxygen transport protein in arthropods and mollusks. Tyrosinase and NspF[7] catalyze the hydroxylation of phenols to *o*-diphenols (monooxygenation) along with the subsequent two-electron oxidation to the corresponding *o*-quinones (oxidoreduction) (Scheme 1, center). In addition, NspF can perform the oxygenation of *o*-aminophenols to nitrosophenols (hydroxyanilinase activity) (Scheme 1, bottom).[7] In contrast, catechol oxidase performs only the oxidoreductase reaction. The side-on peroxo species (**P**) has been observed in all CBC enzymes. However, protein

intermediates beyond **P** are unknown, and the molecular mechanisms for the monooxygenation and oxidoreduction reactions remain unclear.
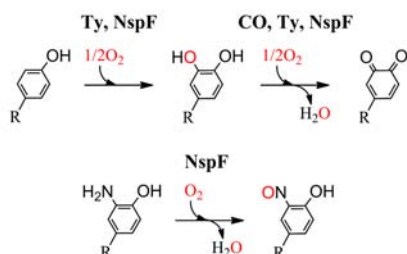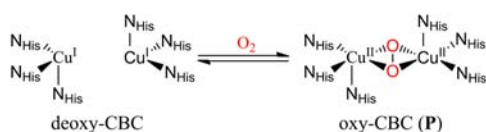
Synthetic models of the CBC active site have shown that Cu(I) can bind O_2 in several different modes.[4,5,8−12] In particular, side-on peroxo Cu(II)₂ (**P**) and bis-μ-oxo Cu(III)₂ (**O**) species have been observed in different ligand systems (Scheme 2).[4,5,8,13] The mode of O_2 binding depends on the nature of the ligand, its coordination geometry (including denticity and sterics),[14] and the type of donor atom (i.e., aliphatic vs aromatic N-ligand, etc.),[15] along with the solvent and counterion.[4,8] In general, more sterically demanding, tridentate ligands favor the **P** species whereas strong σ

Scheme 1

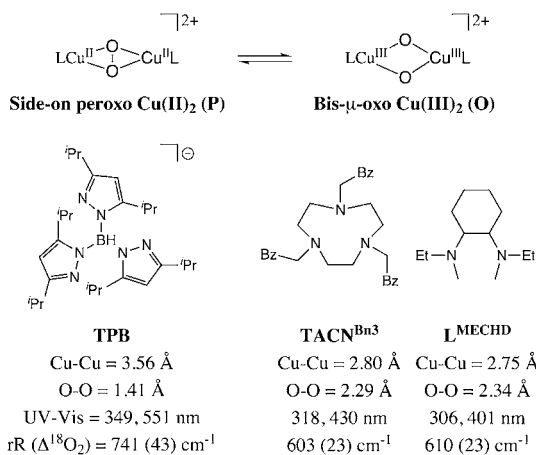Coupled Binuclear Copper (CBC) Proteins: Hc, CO, Ty, NspF

Scheme 2

| TPB	TACN^{Bn3}	L^{MECHD}
Cu–Cu = 3.56 Å	Cu–Cu = 2.80 Å	Cu–Cu = 2.75 Å
O–O = 1.41 Å	O–O = 2.29 Å	O–O = 2.34 Å
UV-Vis = 349, 551 nm	318, 430 nm	306, 401 nm
rR ($\Delta^{18}O_2$) = 741 (43) cm^{-1}	603 (23) cm^{-1}	610 (23) cm^{-1}

donating, bidentate ligands that have limited steric interactions tend to stabilize the **O** isomer.[4,5,16] The first X-ray crystal structure of a **P** species was solved by Kitajima and co-workers with a highly sterically hindered diisopropyl-substituted hydrotris(pyrazolyl)borate (TPB) ligand (Scheme 2, bottom left)[17,18] that revealed a core almost identical to that of **P** found in CBC enzymes.[19,20] Tolman and co-workers solved the crystal structure of the first **O** complex with a tridentate 1,4,7-tribenzyl-1,4,7-triazocyclononane (TACN^{Bn3}) ligand (Scheme 2, bottom center),[21,22] and Stack and co-workers determined a bis-μ-oxo core in a bidentate N,N′-diethyl-N,N′-dimethyl-cyclohexyldiamine (L^{MECHD}) ligand system (Scheme 2, bottom right).[23]

It has also been found that certain **P** complexes can be in rapid equilibrium with the **O** species. Stack and co-workers have demonstrated that the Cu(I) complex of a bidentate ligand, N,N′-di-tert-butyl-ethylenediamine (DBED), reacts with O$_2$ to form a mixture of **P**^{DBED} (~95%) and **O**^{DBED} (~5%) intermediates with the latter being the reactive oxidant in o-hydroxylation.[24,25] Reaction of **P**^{DBED} with a phenolate substrate presumably requires axial phenolate binding to one Cu followed by a trigonal bipyramidal rearrangement of the phenolate into the equatorial Cu$_2$O$_2$ plane. This makes the phenolate a strong donor ligand that leads to O–O bond cleavage and formation of a bis-μ-oxo Cu(III)$_2$-phenolate complex (Scheme 3). This is followed by C–O bond formation

via an electrophilic aromatic substitution (EAS) mechanism. Thus, in the [Cu(II)$_2$(DBED)$_2$(O$_2$)]$^{2+}$ model system, the **O** species is responsible for hydroxylation of the phenolate substrate.[25] In contrast to the above model system, Karlin and co-workers have demonstrated that the [Cu(I)$_2$(NO$_2$-XYL)]$^{2+}$ complex reacts with O$_2$ to exclusively form a **P**$^{NO_2-XYL}$ intermediate that is thought to directly hydroxylate the aromatic ring of the linker (Scheme 4).[26-28]

Scheme 3
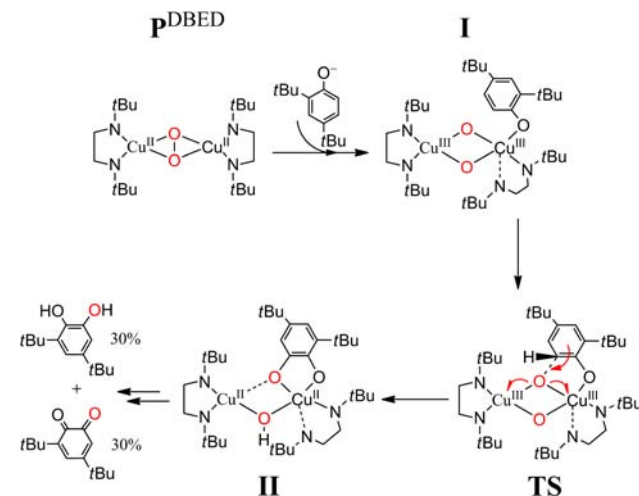
Scheme 4
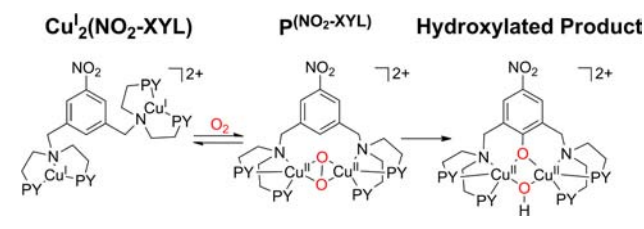
Due to the potential relevance of both the **P** and **O** species to the hydroxylation reaction performed by tyrosinase and NspF, it is important to gain quantitative experimental insight into the electronic structures of these two systems. UV–vis absorption and resonance Raman (rR) spectroscopic studies have demonstrated that the **P** and **O** species have distinct spectral features characteristic of their unique Cu$_2$O$_2$ cores (Scheme 2).[17,23,29] X-ray absorption spectroscopy (XAS), which is a powerful element specific tool for electronic structure determination, was done at the Cu K-edge to reveal side-on peroxo species to be Cu(II) with a pre-edge transition at ~8979 eV, whereas bis-μ-oxo complexes have a pre-edge at ~8981 eV characteristic of Cu(III).[30] Both species, however, are EPR silent with no direct experimental quantification of the copper-dioxygen bonding interactions.

Here, for the first time, we have directly quantified the Cu–O bonding interaction in the **P** and **O** species using Cu L-edge XAS, which provides a sensitive probe of the charge on the copper ions and thus probes the covalent donor interactions of the peroxo and oxo ligands with the Cu centers. Two well-characterized systems, **P**^{TPB} (**1**) (Scheme 2, left) and **O**^{TEED} (**2**) (TEED = N,N,N′,N′-tetraethylethylenediamine, similar to the ligand in Scheme 2, bottom right), are used for the **P** and **O** species, respectively. The experimentally determined electronic

structures of **1** and **2** are used to calibrate density functional theory (DFT) calculations to find the percent Hartree−Fock (HF) mixing required in a functional to quantitatively reproduce the covalent Cu−O bonding interactions. It is important to emphasize that DFT calculations with different amounts of HF mixing have been found to give quantitatively different descriptions of the bonding,[31−33] and the determination of a meaningful reaction coordinate requires an accurate description of the electronic structure.

Using the experimentally calibrated DFT functional, we have investigated the hydroxylation mechanism in the $[Cu(II)_2(NO_2\text{-}XYL)(O_2)]^{2+}$ system that is also a potential model for tyrosinase and NspF.[26,34,35] This model complex is particularly interesting because it allows the study of the *o*-hydroxylation in a system where only the **P** species is present and the substrate does not bind to Cu, in contrast to the phenolate substrate-bonded **O** species in $[Cu_2(DBED)_2(O_2)]^{2+}$. The goal is to determine whether the O−O cleaves along the reaction coordinate forming the **O** species before hydroxylation or whether the **P** intermediate is a viable candidate for hydroxylation in tyrosinase and NspF.

2. EXPERIMENTAL SECTION

2.1. Sample Preparation. The $[\{HB(3,5\text{-}^iPr_2pz)_3Cu\}_2(O_2)]$, **1** (**P**^{TPB}), and $[(L^{TEED}Cu)_2(O_2)]^{2+}$, **2** (**O**^{TEED}), complexes were prepared as described before.[18,36] Both complexes are temperature sensitive and were handled under inert N_2 atmosphere and at dry ice temperatures during sample preparation.

2.2. L-Edge X-ray Absorption Measurements and Data Analysis. For Cu L-edge XAS data collection, the solid samples were spread thinly over double-sided adhesive conducting graphite tape mounted on an Al sample paddle. The paddles were transferred onto a magnetic manipulator in an antechamber prechilled with liquid N_2 and then transferred into the main chamber and affixed to an Al block, which was cooled through conduction by a continuous flow of liquid He into a Cu block in an internal cavity. The temperature was monitored using a Lakeshore temperature controller and maintained at ~50 K during the course of data collection.

Cu L-edge X-ray absorption spectra were recorded at SSRL on the 31-pole wiggler beamline 10-1 under ring operating conditions of 50−100 mA and 3 GeV with a spherical grating monochromator with 1000 lines/mm and set at 30 μm entrance and exit slits. Sample measurements were performed using the total electron yield mode, where the sample signal (I_1) was collected with a Galileo 4716 channeltron electron multiplier aligned to 45° relative to the copper paddle. The signal was intensity-normalized (I_1/I_0) using the photocurrent of a gold grid reference monitor (I_0). Data for all samples were recorded in a sample chamber maintained below 10^{-6} Torr, isolated from the ultrahigh vacuum beamline by a 1000 Å Al window.

External energy calibration was accomplished by L-edge measurements on CuF_2 before and after those of the sample. The L_3 and L_2 peak maxima were assigned to 930.5 and 950.5 eV, respectively. The variance in this calibration energy measured prior to and after each sample scan was used to shift linearly the experimental spectra between calibration scans. Spectra presented here are 3−5 scan averages, which were processed by fitting a second-order polynomial to the pre-edge region and subtracting it from the entire spectrum as background, resulting in a flat postedge. The data were normalized to an edge jump of 1.0 at 1000 eV. The rising edges of the data were subtracted as arctangents. The total area under the L_3 and L_2 peaks was calculated by integrating the intensity between 925 and 955 eV. The integrated area was compared to that for D_{4h} $[CuCl_4]^{2-}$ to obtain per-hole covalency numbers. Complex **2** decomposed to a Cu(II) species during data collection. The data for the pure decomposition Cu(II) product of **2** was also collected and subtracted from that of **2** to

obtain the clean Cu(III) data. This led to a larger error of ±6% in **2** compared to ±4% in **1** for subsequent d-hole character determination.
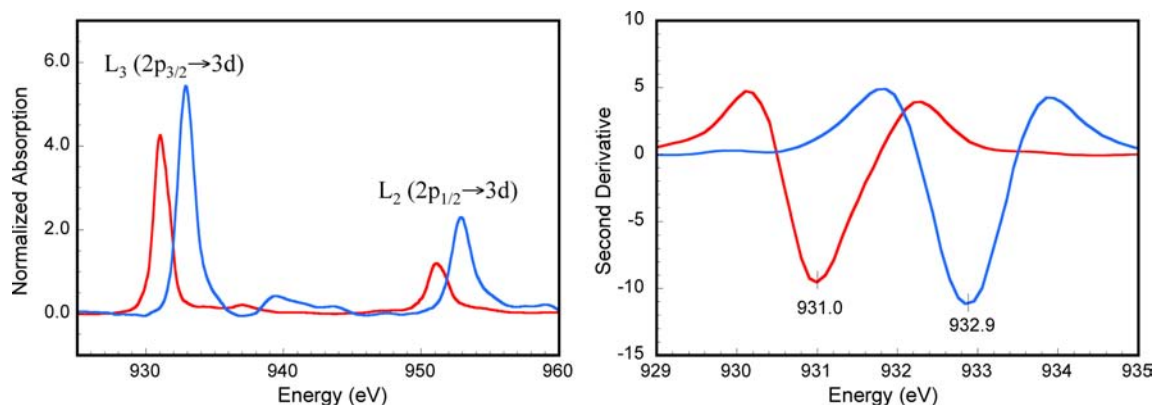
2.3. K-Edge X-ray Absorption Measurements and Data Analysis. The solid samples were ground in boron nitride at liquid N_2 temperature to form a homogeneous mixture that was pressed into a pellet and sealed between Kapton tape windows in a 1 mm aluminum spacer. The samples were maintained below 10 K during data collection using an Oxford Instruments CF 1208 continuous-flow liquid helium cryostat.

Cu K-edge X-ray absorption spectra were measured at SSRL on the unfocused 20-pole, 2.0-T wiggler beamline 7-3 under storage ring parameters of 50−100 mA and 3 GeV. A Rh-coated premonochromator, flat, bent mirror was used for harmonic rejection and vertical collimation. A Si(220) double crystal monochromator was used for energy selection. Transmission data were collected with N_2-gas-filled ionization detector (I_1). Internal energy calibration was accomplished by simultaneous measurement of the absorption of a Cu foil placed between two ionization chambers (I_1 and I_2) situated after the sample. The first inflection point of the foil spectrum was assigned to 8980.3 eV. The energy-calibrated transmission data (I_1/I_0) (k = 13.4 Å^{-1}) were processed by fitting a second-order polynomial to the pre-edge region and subtracting this from the entire spectrum as background. A one-region spline of order 2 was used to model the smoothly decaying postedge region. Normalization of the data was achieved by scaling the spline function and data such that the value of the spline equals 1.0 at 9000 eV. This background subtraction and normalization was done using PySpline.[37,38] Since some photodamage was observed over time, data presented in Supporting Information Figure S1 are the first scans of each data set to eliminate any spectral changes from photo-reduction.

2.4. Computational Details. Spin-unrestricted broken-symmetry (BS) density functional theory (DFT) calculations were performed using the Gaussian 09[39] or ORCA 2.6.35[40] packages. Structures of **1** and **2** were calculated using the pure functional BP86 (Becke GGA exchange[41] with Perdew 1986 nonlocal correlation[42]) and the functional BLYP (Becke GGA exchange[41] with Lee, Yang, and Parr correlation[43,44]) modified to include 10%, 20%, and 38% Hartree−Fock.[45] The B3LYP hybrid functional (with 20% HF mixing)[46] was used to calculate the hydroxylation reaction coordinate, since it gives more accurate electronic structures than BP86, as determined in section 3.2.2. The TZVP basis set was used for the Cu, N, and O atoms. The SVP basis set was used for B, C, and H atoms. For the reaction coordinate analysis TZVP was also used for the *ortho*-C and *ortho*-H that participate in the hydroxylation reaction.

Geometry optimizations of **1** and **2** in vacuum were performed starting from crystallographically derived parameters[18] where the modified crystal structure of $[(L^{MECHD}Cu)_2O_2]^{2+}$[23] (Scheme 2, bottom right) was used for **2**. The crystal structure of $[Cu(II)_2(H\text{-}XYL\text{-}O^-)(OH^-)]^{2+}$[47] was used to optimize the hydroxylated product $[Cu(II)_2(NO_2\text{-}XYL\text{-}O^-)(OH^-)]^{2+}$ with a *para*-NO_2 substituted xylyl. The O···O unit (with O···O = 2.43 Å, Supporting Information Table S9) in the hydroxylated product was further modified into a peroxo (with O−O = 1.42 Å) and optimized to obtain the structure of the **P**$^{NO_2−XYL}$ intermediate. The reaction coordinate for $[Cu(II)_2(NO_2\text{-}XYL)(O_2{}^{2-})]^{2+}$ was calculated from this starting structure of **P**$^{NO_2−XYL}$. The second reaction coordinate studied was for $[Cu(II)_2(NH_3)_4(O_2{}^{2-})]^{2+}$, where the starting side-on peroxo structure was optimized from the modified the crystal structure of **1**.

The self-consistent field (SCF) calculations were set to a tight convergence criterion. All fully optimized structures were verified as minima by frequency calculations that gave no imaginary frequency. The $\nu_{O−O}$ and $\nu_{C−O}$ obtained from the frequency calculations reported here were scaled by a factor of 0.965.[48,49] Transition state (TS) structures were confirmed to have a single imaginary mode corresponding to the reaction coordinate. Intrinsic reaction coordinate (IRC) calculations showed that the TS structures are along the path between the reactants and products. Single point calculations on **P**$^{NO_2−XYL}$ and the transition state structure were performed using the polarizable continuum model (PCM)[50] using the default parameters for CH_2Cl_2 (EPS = 8.93) to check for any effect on $\Delta G^{\ddagger}$. Dispersion

17419

dx.doi.org/10.1021/ja4078717 | *J. Am. Chem. Soc.* 2013, 135, 17417−17431

Figure 1. Cu L-edge XAS spectra of **1** (red line) and **2** (blue line). (Left) Normalized Cu L-edge XAS spectra. The weak edge jumps were simulated with arctangent functions and subtracted from the entire spectrum. The intense peaks at ~930 and ~950 eV represent the L_3-edge ($2p_{3/2} \rightarrow 3d$ transition) and the L_2-edge ($2p_{1/2} \rightarrow 3d$ transition), respectively. (Right) Smoothed second derivative of the Cu L_3-edge region.

and relativistic effects were included using a VDW[51] and DKH[52] Hamiltonian where indicated in the text. QMForge[53] was used to calculate molecular orbital compositions via Mülliken population analysis[54] and for Mayer bond orders.[55,56] Wave functions were visualized, and orbital contours were generated in VMD.[57] The two-dimensional potential energy surfaces were generated in gnuplot.

In agreement with the experimentally determined spin of **P** complexes, **P**$^{NO_2-XYL}$ is well-described by a broken-symmetry (BS) wave function with antiferromagnetically coupled Cu(II)'s, yielding a $M_S = 0$ ground state electronic structure. The BS energies of **P**$^{NO_2-XYL}$ and structures along the reaction coordinate leading to the TS (with BS spin expectation, $\langle S^2 \rangle$, values of 0.7−1.0) were corrected for spin contamination from the triplet ($S_T = 1$) excited state to obtain the singlet ($S_T = 0$) energies using the spin corrected method by Yamaguchi et al. given by eq 1:[58]

$$^1E = \frac{2^{BS}E - \langle S^2 \rangle_{BS}\,^3E}{2 - \langle S^2 \rangle_{BS}} \qquad (1)$$

For the transition state structure and the ones that follow with BS $\langle S^2 \rangle$ values greater than 1.0, due to the formation of additional spins on the xylyl ring and the distal oxygen, the BS energies are contaminated by the triplet ($S_T = 1$) and the quintet ($S_T = 2$) excited states. Equations 1 and 2[59] are used for spin correction for the $S_T = 1$ and $S_T = 2$ excited states, respectively:[59]

$$^1E = \frac{6^{BS}E - \langle S^2 \rangle_{BS}\,^5E}{6 - \langle S^2 \rangle_{BS}} \qquad (2)$$

3. RESULTS AND ANALYSIS

3.1. L-Edge X-ray Absorption Spectroscopy. The normalized, edge subtracted Cu L-pre-edge X-ray absorption spectra of $[\{HB(3,5\text{-}^iPr_2pz)_3Cu\}_2(O_2)]$, **1** (**P**^{TPB}), and $[(L^{TEED}Cu)_2(O_2)]^{2+}$, **2** (**O**^{TEED}), are presented in Figure 1 (left). The second derivatives of the expanded L_3 regions of the spectra of **1** and **2** are shown in Figure 1 (right). The Cu L-edge involves an electric dipole-allowed Cu 2p→3d transition. The $2p^5$ core configuration of the final state undergoes spin−orbit coupling to give two peaks split by ~20 eV, the $J = {}^3/_2$ L_3-edge at ~930 eV and the $J = {}^1/_2$ L_2-edge at ~950 eV with an intensity ratio of ~2:1, respectively.[61] The L_2-edge is ~1.5 times broader than the L_3-edge due to an additional Coster−Kronig Auger decay channel for this excited state.[62] The L_3- and L_2-pre-edge features are followed by weak 2p → 4s and 2p → continuum edge transitions at ~10 eV higher energies (the intensity of the $\Delta l = -1$ transition is ~30 times lower than that of the $\Delta l = +1$ transition). The L_3-edge of **1** occurs at 931.0 eV,

which is equivalent to the energy position of L_3 in D_{4h} $[CuCl_4]^{2-}$ and comparable to L_3 transitions for many tetragonal Cu(II) complexes.[63] The L_3-edge of **2** is at 932.9 eV, shifted 1.9 eV to higher energy, consistent with a change in oxidation state to Cu(III).[64] An analogous trend in energy is observed for the L_2-edge.

The Cu 2p → 3d L-edge intensity can be used to experimentally obtain the amount of unoccupied metal d character in the ground state wave function and thus quantify the copper-dioxygen bonding. Since the Cu 2p orbital is localized on the Cu center and the 2p → 3d transition is electric dipole-allowed, the total intensity of the L_3- and L_2-pre-edges reflects the Cu d character in the Ψ^*_{LUMO}. The oxygen and nitrogen ligand valence 2p orbitals undergo bonding/antibonding interactions with the Cu 3d orbitals leading to the mixing of some ligand 2p character (β^2) into the ground state wave function.[65] Thus, increasing ligand character (covalency) in the ground state decreases the metal 3d character and therefore the intensity of the 2p → 3d Ψ^*_{LUMO} transition by β^2 (eq 3).

$$\Psi^*_{LUMO} = \sqrt{1 - \beta^2}\,|Cu(3d_{x^2-y^2})\rangle - \beta\,|\text{ligand}(np)\rangle \qquad (3)$$

Correlating the L-edge intensity of **1** and **2** with that of the well-characterized D_{4h} $[CuCl_4]^{2-}$ complex (61 ± 4% Cu d character in the $\Psi^*_{\beta\text{-LUMO}}$) gives a quantitative estimate of the amount of Cu unoccupied 3d character in their ground state wave functions. Table 1 lists the Cu characters obtained from the total integrated intensity of the L-edge spectra of **1** and **2**.[66] Accounting for two 3d holes per Cu for **2** and one hole for **1** and D_{4h} $[CuCl_4]^{2-}$, the unoccupied Cu characters of **1** and **2** are 52 ± 4% and 40 ± 6%, respectively. The decrease in Cu d character in **1** and **2** compared to that in D_{4h} $[CuCl_4]^{2-}$

Table 1. Cu L-Edge X-ray Absorption Edge Energies (eV) and Cu Character in Ψ^*_{LUMO} of 1 and 2

	2p → 3d energy[a]		
	L_3-edge	L_2-edge	Cu character in Ψ^*_{LUMO} (% hole)
1	931.0	951.0	52 ± 4
2[b]	932.9	952.8	79 ± 6

[a]Energy resolution is ~0.1 eV. The energy is determined from the minimum intensity of the second derivative. [b]Two-hole system (see text for detail).

indicates stronger covalent mixing of the Cu centers with the ligand (predominantly oxygen) valence orbitals. Furthermore, the higher covalency of **2** relative to **1** indicates that the Cu centers in the O^{TEED} species have a stronger bonding interaction with the oxygen bridging ligands than in the P^{TBP} species, consistent with shorter Cu(III)−O bonds in the O^{TEED} complex (~1.80 Å versus ~1.90 Å).

3.2. Calculations. *3.2.1. Geometric Structure.* It has been established that the amount of Hartree−Fock (HF) mixing in DFT functionals affects calculated geometric and electronic structures.[31,32,67,68] Therefore, we have performed DFT calculations with varying HF mixings to determine the amount that best reproduces geometric and electronic structures of **1** and **2**. Specifically, we have used the pure functional BP86 and BLYP modified with 10%, 20% (B3LYP), and 38% HF mixing to calculate the structures of **1** (Figure 2, left) and **2** (Figure 2, right). Selected structural parameters from the DFT-optimized structures of the two complexes are compared to those obtained from crystallography in Tables 2 and 3, and Supporting Information Tables S1 and S2. The crystal structure of **1** is available,[18] whereas no crystal structure of **2** exists; $[(L^{MECHD}Cu)_2O_2]^{2+}$ (Scheme 2, bottom right) most closely resembles complex **2** and was used for comparison.[23]
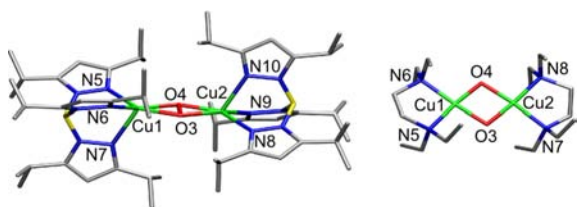
Figure 2. Schematic representations of (left) **1** and (right) **2**. H atoms are omitted for clarity.

Table 2. Comparison of Select Structural Parameters of 1 from DFT Calculations and Crystallography with All Bond Lengths in Å

param	X-ray[18]	BP86	10% HF	B3LYP	38% HF
∠Cu1,O3,O4,Cu2[a]	180.0	174.6	179.8	180.0	179.8
O3−O4	1.413	1.450	1.446	1.457	1.484
Cu1−Cu2	3.556	3.705	3.728	3.718	3.681
av Cu−O	1.914	1.993	1.999	1.997	1.985
av Cu−Neq	1.997	2.007	2.022	2.035	2.058
av Cu−Nax	2.260	2.244	2.283	2.300	2.322

[a]Dihedral angle of the Cu_2O_2 core.

Table 3. Comparison of Select Structural Parameters of 2 from DFT Calculations and Crystallography with All Bond Lengths in Å

param	X-ray[23]	BP86	10% HF	B3LYP	38% HF
∠Cu1,O3,O4,Cu2[a]	173.7	180.0	180.0	180.0	180.0
O3−O4	2.344	2.372	2.363	2.349	2.329
Cu1−Cu2[b]	2.748	2.797	2.781	2.775	2.755
av Cu−O[b]	1.808	1.834	1.825	1.818	1.804
av Cu−N[b]	1.938	2.006	2.008	2.009	2.010

[a]Dihedral angle of the Cu_2O_2 core. [b]EXAFS data of **2** (Cu···Cu = 2.75 Å, Cu−O = 1.80 Å, Cu−N = 1.92 Å).[30]

In the case of complex **1**, the experimental planar Cu_2O_2 core is better reproduced with Hartree−Fock mixing. With BP86,

the Cu_2O_2 core is butterflied by 5.4° (Table 2 ∠Cu1,O3,O4,-Cu2) while inclusion of 10% HF gives a planar structure. The calculated Cu···Cu and O−O distances along the series with increasing HF are characteristic of **P** complexes but are slightly longer than the crystallographic distances (variations in Cu···Cu and O−O along the series are within 0.17 and 0.07 Å, respectively, of the X-ray parameters). A similar variation in the DFT optimized bond lengths of **P** species has been observed before.[15] Based only on these structural parameters there is no significant advantage of any functional.

The calculated structures of **2** show a planar Cu_2O_2 core paralleling the crystal structure of $[(LMECHDCu)_2O_2]^{2+}$. The cores are planar for all **O** species studied to date (Supporting Information Table S3).[21−23,36,69−74] A slight improvement in the bond lengths of the Cu_2O_2 core (Cu···Cu, O···O, and Cu−O) is observed with 20−38% Hartree−Fock mixing. The experimental and calculated difference in the Cu···Cu and O···O distances along the series of differing HF mixing are within 0.05 and 0.03 Å, respectively, and smaller than the difference observed for the **P** complexes. All the other calculated distances of **2** are in reasonable agreement with the crystal structure of $[(L^{MECHD}Cu)_2O_2]^{2+}$ (within ~0.08 Å). Again, there is no significant dependence of the geometric structure on the choice of functional.

3.2.2. Electronic Structure. For coupled binuclear $Cu(II)_2$ systems, the half-occupied d orbitals on the two $Cu_{(1,2)}$ centers form symmetric $(d_1 + d_2)$ and antisymmetric $(d_1 − d_2)$ combinations. In $O_2^{2−}$, the degenerate π^* orbitals are occupied (HOMOs), while the σ^* is unoccupied (LUMO) (Figure 3,
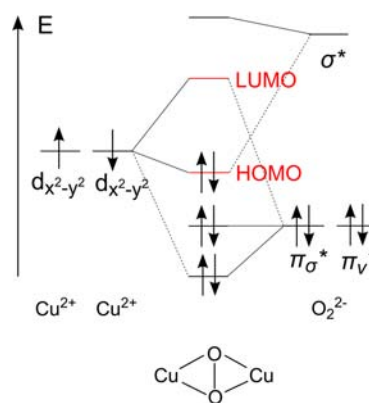
Figure 3. Schematic molecular orbital diagram for **P** species.

right). When $O_2^{2−}$ binds to Cu in **1**, the π^* splits into π_σ^* (orbital in the Cu_2O_2 plane) and π_v^* (orbital out of the Cu_2O_2 plane). The π_σ^* undergoes σ bonding and antibonding interactions with the symmetric combination of Cu $d_{x^2−y^2}$ orbitals to form the HOMO − 2 $[O_2^{2−} \pi_\sigma^* + 2Cu^{2+} (d_{x^2−y^2} + d_{x^2−y^2})]$ and the LUMO $[2Cu^{2+} (d_{x^2−y^2} + d_{x^2−y^2}) − O_2^{2−} \pi_\sigma^*]$, respectively (Figure 3, center and Figure 4, left). The peroxo σ^* similarly forms a bonding and antibonding pair with the antisymmetric combination of filled Cu $d_{x^2−y^2}$ orbitals to form the HOMO $[2Cu^{2+} (d_{x^2−y^2} − d_{x^2−y^2}) + O_2^{2−} \sigma^*]$ and the LUMO + 1 $[O_2^{2−} \sigma^* − 2Cu^{2+} (d_{x^2−y^2} − d_{x^2−y^2})]$, respectively (Figure 3, center and Figure 4, left). The LUMO + 1 peroxo σ^* is 3−6 eV higher in energy than the Cu based LUMO. There is a small amount of backbonding from the occupied Cu d orbitals into the σ^* orbital that results in some σ^* character in the HOMO (Figure 4).
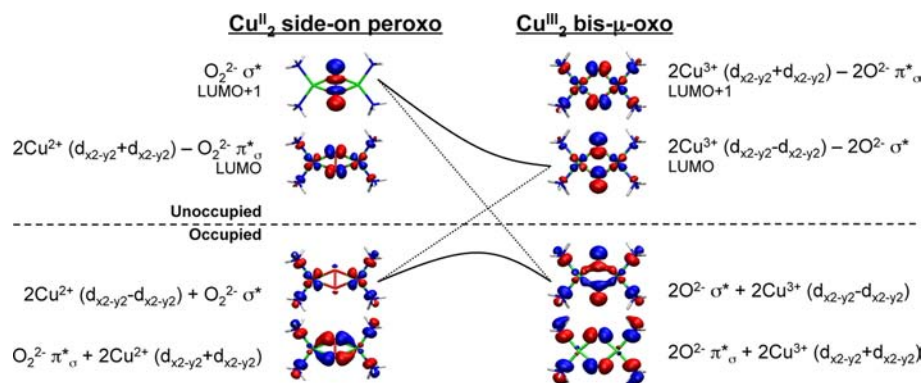
Figure 4. The two key unoccupied MOs and their occupied counterparts in **P** and **O**. The σ^* orbital in **P** has small backbonding from a occupied Cu $d_{x^2-y^2}$ orbital that is not shown here.

As HF mixing is increased, the calculated electronic structure of **1** shows decreasing amounts of σ donation from the filled O_2^{2-} π_σ^* into the symmetric 2Cu ($d_{x^2-y^2}$ + $d_{x^2-y^2}$) LUMO (Supporting Information Table S4). The resulting Cu d-hole character for the different functionals is given in Table 4. The

Table 4. Per Cu Mülliken Population in the α Plus β Unoccupied Orbitals from Spin-Unrestricted Calculations of 1 and 2 with Spin Expectation Values Given in Parentheses

functional	1 (LUMO)	2 (LUMO and LUMO + 1)^a
BP86	45 (0.00)	66 (0.00)
10% HF	49 (0.45)	68 (0.00)
B3LYP	57 (0.61)	71 (0.00)
38% HF	70 (0.90)	76 (0.00)

^{a}Numbers reported here are for two holes per 3d^8 Cu(III).

closest match to the experimental covalency for **1** (52 ± 4% unoccupied Cu character) is obtained with 10–20% HF (49–57% Cu character). The addition of a HF contribution to the functional also leads to spin polarization of the α and β LUMOs as reflected by the increasing spin expectation value

(Table 4) consistent with a Broken Symmetry ($M_S = 0$) singlet ground state. The spin polarized α and β holes reside in the $3d_{x^2-y^2}$ orbitals on each Cu and undergo covalent mixing with the peroxo π_σ^* orbital (Figure 5, left). Spin polarization is not observed with the pure functional (BP86) where both the α and β holes are delocalized over both Cu atoms and the amount of d-hole per Cu is underestimated (45% Cu character) indicating that this functional is too covalent (Figure 5, right). Thus, some HF mixing (10–20%) is required to reproduce the experimental covalency of **1**, which results in spin polarization of the Cu(II)'s consistent with the antiferromagnetically coupled description of **1**.

When **P** isomerizes to **O**, the O–O bond is cleaved. This lowers the peroxo σ^* in energy, oxidizes the Cu(II) to Cu(III), and reduces the O_2^{2-} to $2O^{2-}$ leading to complex **2**.[75] This results in two Cu based LUMOs that are the symmetric and antisymmetric combinations of the Cu $d_{x^2-y^2}$ orbitals and are antibonding with the oxo in-plane 2p orbitals (Figure 4, right). These LUMO and LUMO + 1 are separated by <0.2 eV such that both contribute to the single L pre-edge feature in Figure 1. Note that, in the **P** complex, the σ^* is ∼3–6 eV higher in
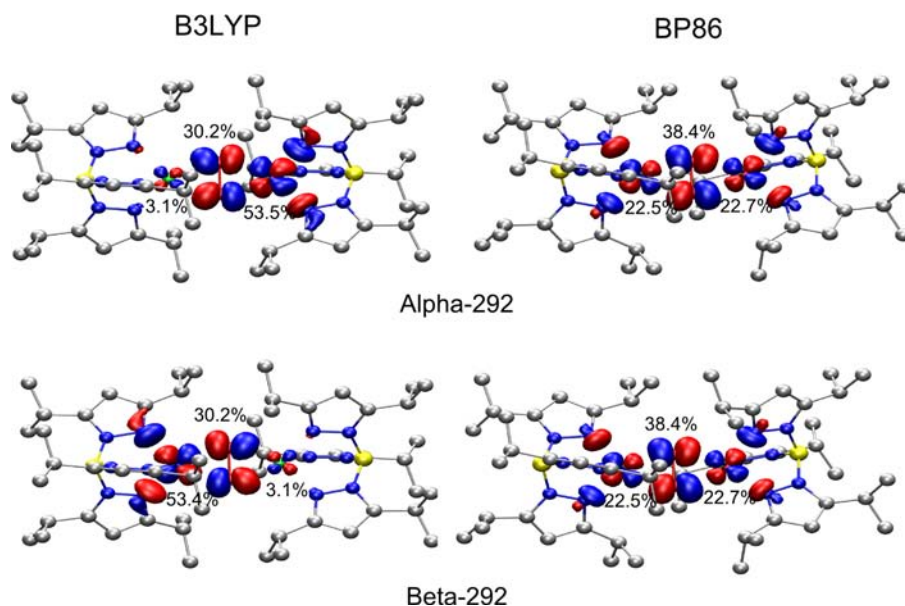
Figure 5. Isosurface plots (isovalue 0.04 au) of α and β LUMO of **1** from B3LYP in the BS ($M_S = 0$) state (left) and BP86 (right) spin-unrestricted calculations.

energy with little Cu character and does not contribute to the pre-edge.

The calculated electronic structure of **2** shows increasing amounts of Cu d character in the LUMO and LUMO + 1 as % HF mixing is increased (Supporting Information Table S5). Table 4 summarizes the total d-hole character per Cu for the different functionals using Mülliken populations. The closest match to the experimental covalency for **2** (79 ± 6% Cu hole) is obtained with 38% HF (77% Cu hole). Both the LUMO and LUMO + 1 are delocalized and highly covalent with 36.4% and 40.4% Cu character, respectively (Figure 6).
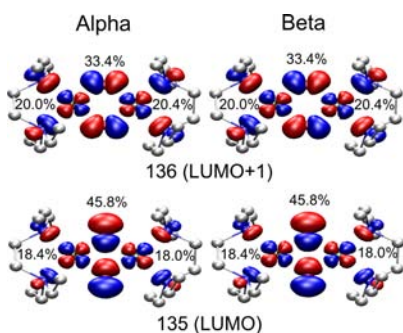
Figure 6. Isosurface plots (isovalue 0.04 au) of α, β LUMO and LUMO + 1 of **2** from 38% HF spin-unrestricted calculations.

Thus, HF mixing is required to reproduce the experimentally observed electronic structures of both **P** and **O** species. The closest agreement with the experimental covalency of **1** is with 10−20% HF, whereas ~38% HF best reproduces that of **2**. We have, therefore, selected B3LYP (with 20% HF) to study the electrophilic aromatic substitution (EAS) reaction coordinate in the $[Cu(II)_2(NO_2\text{-}XYL)(O_2)]^{2+}$ complex to determine the point of O−O bond cleavage with respect to the transition state. To this end, the reaction coordinate obtained for the $\mathbf{P}^{NO_2-XYL}$ structure will be compared with that of the $\mathbf{O}^{DBED}$ complex studied previously with the B3LYP functional as well.[24,25]

3.3. Reaction Coordinate.
3.3.1. P^{NO_2-XYL} Intermediate and Hydroxylated Product. In order to evaluate the EAS reaction coordinate of $[Cu(II)_2(NO_2\text{-}XYL)(O_2)]^{2+}$, we first obtained the geometry optimized structures of the $\mathbf{P}^{NO_2-XYL}$ reactant and the hydroxylated product $[Cu(II)_2(NO_2\text{-}XYL$-

$O^-)(OH^-)]^{2+}$. The calculated ν_{O-O} for $\mathbf{P}^{NO_2-XYL}$ (Figure 7A) is 879 cm^{-1} (the experimental ν_{O-O} is 747 cm^{-1})[28,76,77] and described with a BS singlet ($M_S = 0$) ground state with spin polarized α (2% Cu$_1$ and 48% Cu$_2$ in the LUMO) and β holes (48% Cu$_1$ and 2% Cu$_2$ in the LUMO) in the $3d_{x^2-y^2}$ orbital on each Cu (Supporting Information Table S6). The total Cu character is consistent with Cu L-edge XAS data for **1** (Table 1). Selected structural parameters are given in Supporting Information Table S8 ($\mathbf{P}^{NO_2-XYL}$). The Cu$_2$O$_2$ core is butterflied to 138° to accommodate the xylyl bridge and is consistent with the split O_2^{2-} $\pi_\sigma^* \rightarrow$ Cu charge transfer transitions (360 and 435 nm) from absorption studies.[28,77] The Cu−Cu and O−O distances are 3.57 and 1.42 Å, respectively, while the average Cu−O bond length is 2.04 Å. These distances are characteristic of **P** species.[15] The distance between the proximal oxygen (O$_3$) and the nearest *ortho*-carbon of the arene (C$_{12}$) is 2.79 Å. On the basis of this unconstrained structure, the C−O and O−O distances of 2.80 and 1.42 Å, respectively, were used as the starting point for a scan of the two-dimensional reaction coordinate presented in section 3.3.2.

The final hydroxylated product $[Cu(II)_2(NO_2\text{-}XYL\text{-}O^-)\text{-}(OH^-)]^{2+}$ formed in the EAS reaction (Figure 7B) (see section 3.3.3) has the O−O bond cleaved with a calculated distance of 2.43 Å (crystallographic O−O = 2.43 Å[47]).[78] The C−O bond is fully formed at 1.33 Å (crystallographic C−O = 1.33 Å), and the phenolate product bridges the two Cu(II) centers. All other calculated structural parameters compare well with the crystal structure (Supporting Information Table S9). The Cu$_2$O$_2$ core and the resulting phenolate are nearly planar (∠CuOOCu = 177°$_{calc}$, 178°$_{x-ray}$; ∠C$_{15}$C$_{12}$O$_3$ = 180°$_{calc}$, 178°$_{x-ray}$). The experimental ν_{C-O} of 1320 cm^{-1} is in good agreement with the calculated frequency of 1302 cm^{-1}.[28] Formation of this hydroxylated product will be discussed in section 3.3.3.

3.3.2. Two-Dimensional Reaction Coordinate of O−O Bond Cleavage and C−O Bond Formation. Reaction of the $\mathbf{P}^{NO_2-XYL}$ intermediate (Figure 7A) to form the hydroxylated product $[Cu(II)_2(NO_2\text{-}XYL\text{-}O^-)(OH^-)]^{2+}$ (Figure 7B) requires cleavage of the O$_3$−O$_4$ and C$_{12}$−H$_{11}$ bonds and formation of the C$_{12}$−O$_3$ and O$_4$−H$_{11}$ bonds. In section 3.3.3, it is shown that the cleavage of the C$_{12}$−H$_{11}$ bond (and the subsequent formation of the O$_4$−H$_{11}$ bond) occurs after the transition state for C$_{12}$−O$_3$ formation, consistent with the experimental kinetic isotope effect of ~1.0. In this section, the cleavage of the O$_3$−O$_4$ and formation of the C$_{12}$−O$_3$ bonds are
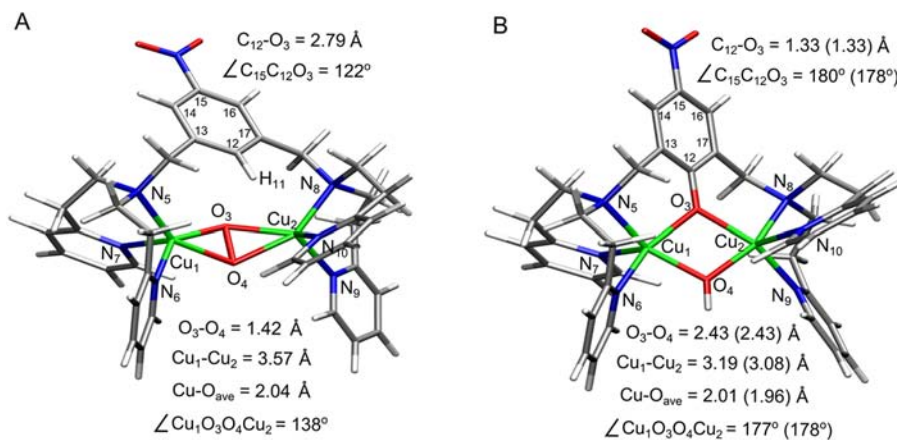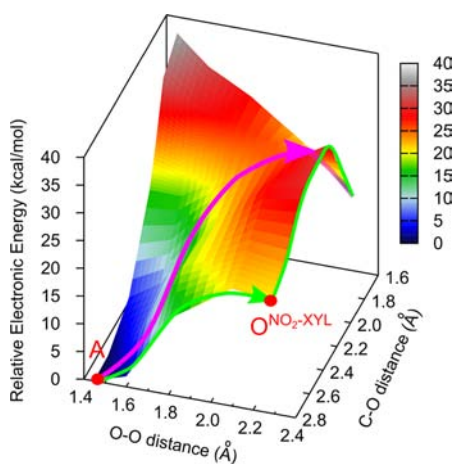

Figure 7. B3LYP optimized structures of (A) the $\mathbf{P}^{NO_2-XYL}$ complex, and (B) the final hydroxylated product $[Cu(II)_2(NO_2\text{-}XYL\text{-}O^-)(OH^-)]^{2+}$. Crystallographic parameters are given in parentheses.
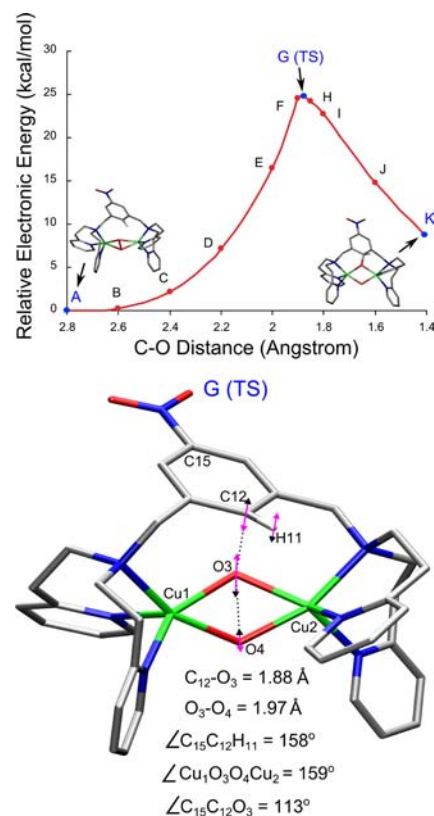
evaluated. The two-dimensional potential energy surface (PES) of the electronic energy as a function of the O_3–O_4 and C_{12}–O_3 distances is presented in Figure 8. The C_{12}–O_3 was decreased in steps of 0.20 Å from 2.80 to 1.60 Å, and for every point the O_3–O_4 bond was elongated (1.45, 1.60, 1.80, 2.10, and 2.28 Å). This 2D PES compares the energetics of the two possible reaction pathways: (i) concerted reaction where the C_{12}–O_3 forms concurrently with O_3–O_4 cleavage (pink curve in Figure 8) and (ii) stepwise reaction where the C_{12}–O_3 forms after complete O_3–O_4 cleavage (green curve in Figure 8). Figure 8 shows that the concerted reaction is energetically favorable and gives the lowest energy route on the PES (pink curve). The alternate route of first forming $\mathbf{O}^{NO_2-XYL}$ (followed by C_{12}–O_3 bond formation) (green curve) is higher in energy by ∼20 kcal/mol. The lowest energy route (pink line) is replotted in Figure 9, top, with additional points added near the transition state (TS) and at the end point **K** (the unconstrained species with C_{12}–H_{11} still present) with a C_{12}–O_3 of 1.41 Å.

TS Geometric and Electronic Structure. The transition state along the C_{12}–O_3 bond formation reaction coordinate occurs at a C_{12}–O_3 distance of 1.88 Å (**G**) (Figure 9, top). This has one imaginary frequency of −547 cm^{-1} [with a displacement ratio of $(0.63\ O_3):(−0.25\ O_4):(−0.48\ C_{12}):(0.44\ H_{11})$] (Figure 9, bottom, magenta arrow) showing O_3–O_4 bond cleavage occurs concurrently with C_{12}–O_3 bond formation. The calculated energy barriers, ΔH and ΔG, corrected for spin contamination, are ∼24 kcal/mol and ∼26 kcal/mol, respectively. When dispersion and relativistic effects are also included,[79,80] the barrier height is lowered by ∼5 kcal/mol and within DFT accuracy of the experimental activation energies (experimental $\Delta H^{\ddagger}$ = 13 ± 2 kcal/mol, $\Delta G^{\ddagger}$ = 15 ± 2 kcal/mol).[28,81,82] An intrinsic reaction coordinate (IRC) calculation confirms that the TS is along the EAS reaction coordinate.

In going from point **A** to the TS structure (**G**), the O_3–O_4 distance increases from 1.42 to 1.97 Å while the Cu_1–Cu_2 distance decreases from 3.57 to 3.29 Å (Supporting Information Table S8). A decrease in the Cu–O distances is also observed (Cu–O_{av} is 2.04 Å at point **A** and 1.94 Å at point

Figure 9. (Top) Potential energy surface of the formation of phenolate along the C_{12}–O_3 coordinate for $[Cu(II)_2(NO_2\text{-}XYL)\text{-}(O_2)]^{2+}$ extracted from the lowest energy path of the 2D PES (Figure 8, pink line) along O_3–O_4 and C_{12}–O_3 distances with additional points added near the transition state (TS) and at the end point **K**. All hydrogens except H_{11} are omitted for clarity. (Bottom) Transition state structure for C_{12}–O_3 bond formation. The pink arrows represent the mode of the imaginary frequency of −547 cm^{-1} with the length of the arrows representing the relative displacement of the atoms.

G, Supporting Information Table S8). The key angles to note are the $\angle Cu_1O_3O_4Cu_2$ dihedral angle of the Cu_2O_2 core that becomes more planar (138° at point **A** and 159° at point **G**) and the phenolate angle ($\angle C_{15}C_{12}O_3$) that becomes more perpendicular (122° at point **A** and 113° at point **G**). Another important geometric change observed at the TS is distortion of C_{12} of the xylyl ring from a planar sp^2 to a pseudotetrahedral sp^3 hybridized state ($\angle C_{15}C_{12}H_{11}$ is 177° at point **A** and 158° at point **G**). The C_{12}–H_{11} bond distance decreases consistently from 1.079 Å at point **A** ($\nu_{(C-H)}$ = 3209 cm^{-1}) to 1.075 Å (at point **D**) before the TS, and at the TS it increases slightly to 1.080 Å ($\nu_{(C-H)}$ = 3195 cm^{-1}) and continues to increase (Supporting Information Table S8). The kinetic isotope effect (KIE) is calculated to be 1.00, which matches the experimentally observed KIE of ∼1.0.[83,27]

Changes in the electronic structure from point **A** to **G** were investigated by monitoring the Mayer bond order (MBO) (Table 5) that shows that as the C_{12}–O_3 bond is strengthened, the O_3–O_4 bond is weakened. To obtain a reference for a full C–O bond, structure **K** was reoptimized with the C_{12}–H_{11} proton removed (structure **L**, C_{12}–O_3 MBO of 1.180) (Table 5).[84] The O–O MBO of structure **A** (0.733) is used as the reference for an unperturbed side-on peroxo O–O bond. Thus, at the TS, the C_{12}–O_3 is found to be 25% formed while 63% of the O–O bond is broken (the TS of the EAS reaction for

Figure 8. Two-dimensional potential energy surface (PES) showing electronic energy changes as a function of O_3–O_4 and C_{12}–O_3 distances for $[Cu(II)_2(NO_2\text{-}XYL)(O_2)]^{2+}$. The pink line indicates the lowest energy route on the PES from **A**, the 2.80 Å C_{12}–O_3 $\mathbf{P}^{NO_2-XYL}$ starting structure, leading to **K**, the end species (not shown here). The green line indicates the path taken to first form $\mathbf{O}^{NO_2-XYL}$ followed by C_{12}–O_3 bond formation.

Table 5. Distances and Mayer Bond Order (MBO) for C_{12}–O_3 and O_3–O_4 along the C_{12}–O_3 Coordinate for $[Cu(II)_2(NO_2\text{-}XYL)(O_2)]^{2+}$

structure	C_{12}–O_3 Å	C_{12}–O_3 MBO	O_3–O_4 MBO	CO formed %	OO formed %
A	2.800	<0.01	0.733		100
B	2.600	<0.01	0.723		99
C	2.400	<0.01	0.709		97
D	2.200	<0.01	0.688		94
E	2.000	<0.01	0.635		87
F	1.900	0.030	0.572	3	78
G (TS)[a]	1.880	0.296	0.272	25	37
H	1.850	0.426	0.133	36	18
I	1.800	0.511	0.095	43	13
J	1.600	0.730	0.035	62	5
K[a]	1.409	0.893	<0.01	76	
L[b]	1.303	1.180	<0.01	100	

[a]Fully optimized structures with no constraints. [b]Optimized structure with C_{12}–H_{11} broken and H^+ removed.

$[(DBED)_2Cu(III)_2(O^{2-})_2]^{2+}$ had 27% of the C–O bond formed while the O···O bond was fully broken[25]).

Inspection of the Mülliken charge and spin densities on the different fragments [Cu_1, Cu_2, O_3, O_4, xylyl-ring (NO_2–C_6H_3), and rest of the ligand] provides insight into the electronic structure changes that occur along the reaction coordinate (Tables 6 and 7, and Supporting Information Tables S10 and

Table 6. Mülliken Charge of Key Species along the C_{12}–O_3 Coordinate for $[Cu(II)_2(NO_2\text{-}XYL)(O_2)]^{2+}$

	2.80 A	1.88 G (TS)[a]	1.409 K[a]
Cu_1	0.38	0.41	0.40
Cu_2	0.37	0.44	0.42
O_3	−0.25	−0.42	−0.48
O_4	−0.23	−0.35	−0.31
(NO_2–C_6H_2)	−0.05	0.13	0.06
H_{11}	0.07	0.12	0.12
rest	1.78	1.80	1.90

[a]Fully optimized structures with no constraints.

Table 7. Mülliken Spin and Spin Expectation of Key Species along the C_{12}–O_3 Coordinate for $[Cu(II)_2(NO_2\text{-}XYL)(O_2)]^{2+}$

	2.80 A	1.88 G (TS)[a]	1.409 K[a]
Cu_1	0.44	0.52	0.59
Cu_2	−0.44	−0.52	−0.57
O_3	0.02	−0.21	−0.03
O_4	−0.01	0.52	0.96
(NO_2–C_6H_2)	0.00	−0.31	−0.98
H_{11}	0.00	0.02	−0.07
rest	−0.01	−0.01	0.03
$\langle S^2 \rangle$	0.87	1.10	1.95

[a]Fully optimized TS and K end species with no constraints.

S11). The two Cu centers remain spin polarized and antiferromagnetically coupled from points **A** to **G** (+0.52 spin on Cu_1 and −0.52 spin on Cu_2 at point **G**, Table 7) and thus are described as Cu(II) centers.[85] It is important to note that the xylyl ring becomes noticeably positive with the Mülliken charge increasing from +0.02 at point **A** to +0.25 at point **G** [Table 6, combined charge on fragments (NO_2–C_6H_2) and

H_{11}]. In addition, at point **G** there is a net β spin of −0.29 on the xylyl ring whereas the net spin at point **A** is 0.00 [Table 7, combined spin on fragments (NO_2–C_6H_2) and H_{11}]. This increase in positive Mülliken charge and β spin on the xylyl ring is due to a 23% α electron donation from the π electron cloud of the xylyl ring (Table 8) (Figure 10, orbital 188α in **A**) into

Table 8. Change in Mülliken Population of the Filled Orbitals along the C_{12}–O_3 Coordinate Compared to Structure A[a]

	G (1.88)		K (1.409)	
	α	β	α	β
Cu_1 (d orbitals)	−2	−9	1	−16
Cu_2 (d orbitals)	−9	−3	−13	−3
O_3 (p orbitals)	0	24	16	22
O_4 (p orbitals)	34	−17	50	−41
(NO_2–C_6H_3)	−23	5	−54	38

[a]All numbers are in percent of an electron.

the O_2^{2-} σ^* orbital (Figure 10, orbital 210α in **A**)[86] forming orbital 197α at point **G** (Figure 10). Thus, at the TS, the O_3–O_4 weakens due to α electron donation from the xylyl ring. As the peroxide elongates and starts to cleave, the holes on the O_2^{2-} σ^* orbital are spin polarized leading to a partial β hole on the distal O_4 (+0.52 α spin) and a partial α hole on the proximal O_3 (−0.21 β spin) (Table 7). The α hole on the O_3 is smaller than the β hole on the distal O_4 because of the α electron donation from the xylyl ring to O_3. Thus, at the TS the C_{12}–O_3 bond is strengthened while the O_3–O_4 bond is weakened in a concerted manner due to the transfer of partial α electron density from the ring into the O_3–O_4 bond.

Species K. From the TS to the end of the reaction before H_{11} is lost as a proton, the optimized C_{12}–O_3 decreases from 1.88 Å at point **G** to 1.41 Å at point **K**. The O_3–O_4 distance increases from 1.97 to 2.49 Å from point **G** to **K** while the C_{12}–H_{11} has elongated from 1.08 Å in **G** to 1.12 Å in **K** (Supporting Information Table S8). The Cu_2O_2 core becomes mostly planar with the $\angle Cu_1O_3O_4Cu_2$ dihedral angle increasing from 159° at point **G** to 174° at point **K**. In addition, the phenolate angle ($\angle C_{15}C_{12}O_3$ in Figure 11) increases from 113° at point **G** to 145° at point **K** (Supporting Information Table S8) but is still not planar. This bent phenolate angle has an important role that will be explored below.

Inspection of the electronic structure at point **K** reveals that the two Cu centers continue to be spin polarized (+0.59 spin on Cu_1 and −0.57 spin on Cu_2, Table 7) with no increase in Mülliken charge (Table 6) and thus remain antiferromagnetically coupled Cu(II) centers. The β spin character on the xylyl ring has increased to −0.98 while the α spin character on the distal O_4 has increased to +0.96 (Table 7). The increase in β spin density on the xylyl ring is due to an additional 31% α electron donation (Table 8) from the ring to the O_3–O_4 from point **G** to **K**, leaving an α hole in a phenolate-like orbital on the ring (Figure 10 K, orbital 198α and a β spin character of −0.98). The increase of α spin character on the distal O_4 is a result of the complete cleavage of the O_3–O_4 bond that leads to full spin polarization of the O···O σ^* with the α and β holes localized on O_3 and O_4, respectively. Another important change in the electronic structure at point **K** is that the overall Mülliken charge on the xylyl ring has decreased from 0.25 at the TS to 0.18 (Table 6). This decrease in charge on the ring is due to β
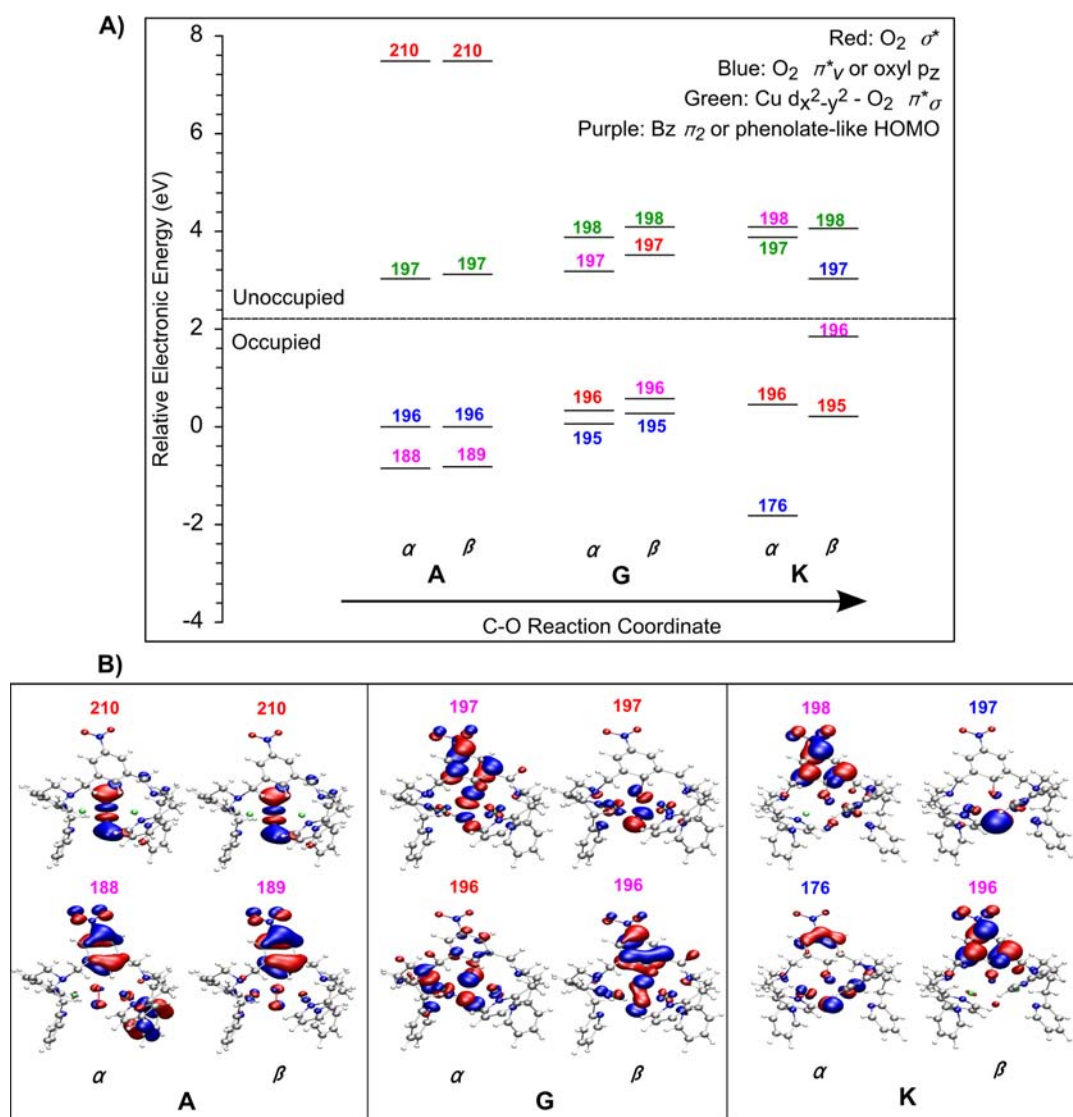
Figure 10. Key orbitals along the $C_{12}-O_3$ reaction coordinate for $[Cu(II)_2(NO_2-XYL)(O_2)]^{2+}$. The unoccupied peroxo σ^* orbitals (210 α, β in **A**) are lowered in energy along the coordinate. An α electron is donated from the occupied xylyl HOMO (orbital 188 in **A**) to the peroxo σ^* orbital leaving an α hole on the xylyl (orbital 198 α in **K**). The β hole ends up on the distal O_4 (oxyl p_z-like orbital, 197β in **K**; the z-axis is perpendicular to the Cu_2O_2 plane).
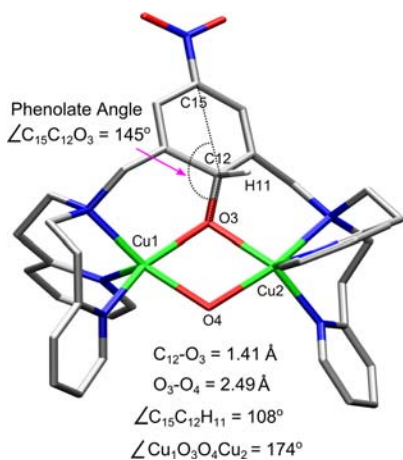
Figure 11. Structure of species **K**. All hydrogens except H_{11} are omitted for clarity.

electron donation from O_3 to form the $C_{12}-O_3$ bond with 38% of the electron density residing on the xylyl ring (Table 8). Thus, the α and β electrons from the xylyl ring and O_3, respectively, pair for the concerted $C_{12}-O_3$ bond formation with O_3-O_4 bond cleavage. However, only 76% of the $C_{12}-O_3$ is formed with the O_3-O_4 completely broken (Table 5) as the $C_{12}-H_{11}$ bond is still present. The $C_{12}-H_{11}$ bond cleavage is explored in section 3.3.3.

1 versus 2 Electron Donation from Substrate. At the end of the above reaction coordinate at point **K**, a partial α electron has been transferred from the xylyl ring to the $O\cdots O$ forming an antiferromagnetically coupled diradical pair with a β spin on the xylyl ring (substrate) and an α spin on the distal O_4. Interestingly, when an unconstrained benzene was used as the substrate for this reaction using a side-on peroxo $[Cu(II)_2(NH_3)_4(O_2^{2-})]^{2+}$ structure as a model (species **X** in Figure 12, Supporting Information Table S13), the species formed at the end of the reaction and before C−H bond cleavage had no diradical character on the substrate and distal
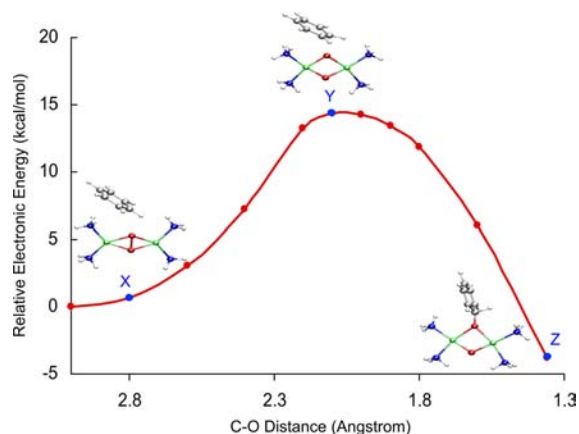
Figure 12. Potential energy surface for the EAS reaction of benzene with $[Cu(II)_2(NH_3)_4(O_2^{2-})]^{2+}$.

O_4 (species **Z** with a C–O distance of 1.36 Å in Figure 12, Supporting Information Tables S13 and S15). Evaluation of the reaction coordinate for $[Cu(II)_2(NH_3)_4(O_2^{2-})]^{2+}$ reveals that the side-on peroxo species **X** does react with the substrate to proceed through a transition state, **Y**, with a small amount of diradical character on the aromatic substrate (spin of +0.23) and the distal O_4 (spin of −0.19) (Supporting Information Table S15) and a phenolate angle, ∠CCO, of 119° (Supporting Information Table S13, point **Y** with a C–O distance of 2.08 Å).[87] The diradical character, however, disappears farther along the reaction as the substrate rotates (∠CCO = 163° at point **Z**, Figure 13, right) to allow the second π electron of the HOMO
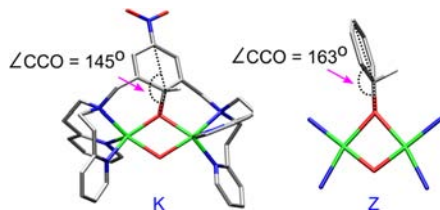
**Figure 13.** Structures of species **K** versus **Z** formed at the end of the EAS reaction coordinates for $[Cu(II)_2(NO_2\text{-}XYL)(O_2)]^{2+}$ and $[Cu(II)_2(NH_3)_4(O_2^{2-})]^{2+}$, respectively, but before *ortho*-H⁺ cleavage. All hydrogens except *ortho*-H are omitted for clarity.

orbital on the ring to overlap the peroxo based LUMO leading to α, β electron pair donation from the substrate.[88] Thus, the only spins observed are the two antiferromagnetically coupled Cu centers (+0.53 on Cu_1 and −0.54 on Cu_2, Supporting Information Table S15) that remain Cu(II) throughout the reaction coordinate.[89] If at point **Z** (Figure 12) the benzene ring is constrained with respect to the Cu_2O_2 plane to a ∠CCO of 145°, consistent with the covalently linked xylyl ring of $[Cu(II)_2(NO_2\text{-}XYL)(O_2)]^{2+}$ at point **K** (Figure 13, left), the species does contain diradical character. Upon removing the constraint on the ring in this spin polarized complex, the ring rotates by ~20° allowing a second electron to transfer and eliminate the diradical character.[90]

3.3.3. $C_{12}–H_{11}$ Cleavage and Completion of the Reaction. In order to fully form the hydroxylated product $[Cu(II)_2(NO_2\text{-}XYL\text{-}O^-)(OH^-)]^{2+}$, the $C_{12}–H_{11}$ proton was removed and the distal O_4 protonated. However, due to the large distance between H_{11} and O_4, an exogenous proton acceptor is potentially needed to facilitate this transfer. In these

calculations, methylamine is used as a model for this exogenous base.[91] Op't Holt et al. showed that the use of stronger/weaker proton acceptors did not significantly change the reaction coordinate.[25] The effect of the $C_{12}–H_{11}$ bond cleavage was modeled with a 2D PES by adding methylamine to the nine structures from **C** to **K** in Figure 9 ($C_{12}–N_{methylamine}$ constrained to 2.80 Å) with the lone pair on the N pointing toward the *ortho*-H_{11}. For each of the nine structures, the N–H_{11} distance was scanned from 2.06, 1.80, 1.60, 1.40, 1.20, to 1.03 Å, resulting in cleavage of the $C_{12}–H_{11}$ bond. The 2D PES of the electronic energy calculated as a function of the $C_{12}–O_3$ and $N_{base}–H_{11}$ bond distances is shown in Figure 14. The
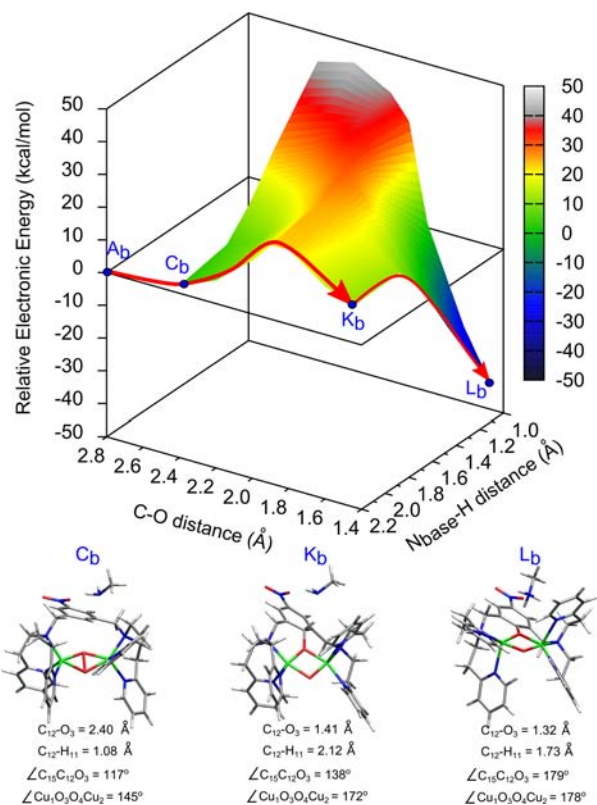
Figure 14. Two-dimensional potential energy surface (PES) for $[Cu(II)_2(NO_2\text{-}XYL)(O_2)]^{2+}$ showing electronic energy changes as a function of $C_{12}–O_3$ and $N_{base}–H_{11}$ distances with methylamine as the base. The red line indicates the lowest energy route on the PES starting from A_b through C_b to K_b and finally forming the deprotonated species L_b. L_b is ~41 kcal/mol lower in energy than A_b.

electronic energy is scaled relative to that of A_b ($C_{12}–O_3 = 2.80$ Å; $C_{12}–H_{11} = 1.08$ Å), which has the same structure as **A** in Figure 9 but with base present (base is also present in structures C_b, K_b, and L_b). The lowest energy path (red line) from C_b ($C_{12}–O_3 = 2.40$ Å; $C_{12}–H_{11} = 1.08$ Å) to K_b ($C_{12}–O_3 = 1.41$ Å; $C_{12}–H_{11} = 1.12$ Å) has essentially the same geometric and electronic structures as those without base present in Figure 9. Thus, the TS state remains unchanged in the presence of a base.

When the $C_{12}–O_3$ bond is constricted sufficiently to 1.41 Å (K_b), it becomes energetically favorable for the proton to be transferred to the nearby base forming structure L_b ($C_{12}–O_3 = 1.32$ Å; $C_{12}–H_{11} = 1.73$ Å), which is ~41 kcal/mol lower in energy than A_b. Along the reaction coordinate from K_b to L_b (Supporting Information Tables S16–18), the diradical

character on the xylyl ring and distal O_4 disappears as the $C_{12}-H_{11}$ bond is elongated from 1.12 to 1.25 Å and the ∠CCO becomes more planar (Supporting Information Table S18). This reflects the additional transfer of the second electron from the xylyl ring (Figure 10 **K**, orbital 196β) to the hole on the distal O_4 (Figure 10 **K**, orbital 197β). Further $C_{12}-H_{11}$ bond elongation to 1.73 Å in $\mathbf{L_b}$ completes $C_{12}-O_3$ bond formation (MBO of 1.18).

Finally, transfer of a proton from the base to the distal O_3 gives another ~40 kcal/mol energy stabilization. Thus, formation of the hydroxylated species $[Cu(II)_2(NO_2\text{-}XYL\text{-}O^-)(OH^-)]^{2+}$ via a base is energetically favorable. The hydroxylated species formed has a structure that is very similar to that of $\mathbf{L_b}$. Protonation of the distal O, therefore, has no substantial effect on the Cu_2O_2 core.

4. DISCUSSION

L-edge XAS experimentally quantified the amount of Cu character in the ground state wave function (Cu 3d character in the unoccupied orbitals) to be 52 ± 4% in **1** ($\mathbf{P^{TPB}}$) and 79 ± 6% in **2** ($\mathbf{O^{TEED}}$). The 52% Cu character in **1** corresponds to one hole per Cu(II) center, whereas, the 79% Cu character in **2** corresponds to two holes per Cu(III) center. The lower per-hole Cu character and thus higher covalency in **2** compared to **1** indicates that the bis-μ-oxo core has a stronger bonding interaction with the Cu centers. The results from L-edge XAS have been correlated to DFT calculations to determine that a HF mixed hybrid functional is required to reproduce the quantitative electronic structures of **1** and **2**. In addition to increasing the Cu 3d-hole character, inclusion of HF mixing leads to spin polarization in **1** with each hole localized on a different Cu. Thus, HF mixing is required to produce the singlet ground state with an antiferromagnetically coupled pair of Cu(II) centers (Figure 5).

B3LYP (with 20% HF), which gives a reasonable comparison to the L-edge XAS data for **1** and **2**, was then employed to evaluate the EAS reaction coordinate in $[Cu(II)_2(NO_2\text{-}XYL)(O_2)]^{2+}$ that has an experimentally defined **P** intermediate. Stack and co-workers have previously shown that the **O** isomer in $[(DBED)_2Cu_2(O_2)]^{2+}$, another potential tyrosinase model, is capable of performing aromatic hydroxylation.[24,25] The goal here was to determine whether the $\mathbf{P^{NO_2-XYL}}$ in $Cu(II)_2(NO_2\text{-}XYL)(O_2)]^{2+}$ converts to an $\mathbf{O^{NO_2-XYL}}$ intermediate along the reaction coordinate for EAS. This is an ideal system to study because the substrate does not bind to the Cu, in contrast with the $[(DBED)_2Cu(III)_2(O_2)]^{2+}$ system, where the phenolic substrate binds to one of the Cu centers and then undergoes EAS. Two key differences are observed in comparing the reaction coordinate of $[Cu(II)_2(NO_2\text{-}XYL)(O_2)]^{2+}$ to the previously developed model of $[(DBED)_2Cu(III)_2(O)_2]^{2+}$. First, the calculations show that, for $[Cu(II)_2(NO_2\text{-}XYL)\text{-}(O_2)]^{2+}$, the Cu centers remain antiferromagnetically coupled Cu(II) throughout the reaction and are not oxidized to Cu(III). The aromatic ring of the cross-linker transfers π electron density directly to the peroxo σ^* orbital resulting in O−O bond cleavage with concerted C−O bond formation (Scheme 5). Thus, the **P** intermediate is best interpreted to be the reactive species in $[Cu(II)_2(NO_2\text{-}XYL)(O_2)]^{2+}$ that performs the EAS reaction.

Second, instead of transferring a pair of electrons from the aromatic ring in $[Cu(II)_2(NO_2\text{-}XYL)(O_2)]^{2+}$ to form the C−O bond, α and β electrons are transferred from the xylyl ring and the peroxo π^*, respectively, due to the limited flexibility of the

Scheme 5
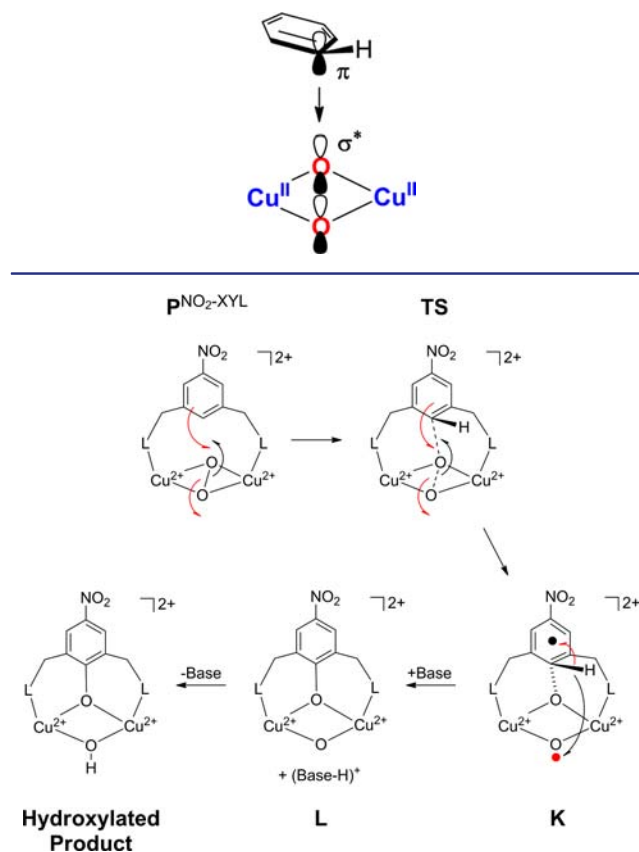
Figure 15. Schematic mechanism of aromatic hydroxylation performed by $\mathbf{P^{NO_2-XYL}}$ in $[Cu(II)_2(NO_2\text{-}XYL)(O_2)]^{2+}$. The red and black arrows represent transfer of α and β electrons, respectively. In going through the transition state (TS) to **K**, a pair of α and β electrons are transferred from the xylyl ring and peroxo π^* orbital, respectively, to concertedly form the C−O bond and cleave the O−O bond. This produces an α spin on O_d that is paired with the β radical on the ring. In proceeding from **K** to **L** and subsequently to the hydroxylated product, the o-H$^+$ is transferred to the O_d via a base. As the o-C−H bond is cleaved, its α and β electrons are transferred to the phenolate and O_d, respectively, leading to the full formation of the phenolate C−O bond.

xylyl chelate (Figure 15). The α counterpart of the peroxo π^* ends up on the distal oxygen (O_d) resulting in a radical on the ring and a radical on O_d that are antiferromagnetically aligned. This diradical character is eliminated as the o-C−H cleaves and a second electron is transferred from the ring to O_d via the O_p-Cu-O_d bonding network. This one versus two electron attack is due to the ∠CCO phenolate angle (Figure 13). In $[Cu(II)_2(NO_2\text{-}XYL)(O_2)]^{2+}$, where the rotation of the aromatic ring is constrained by covalent linkage to be less than 145°, only one electron transfer to peroxide is observed. As the ∠CCO becomes more planar with weakening of the o-C−H bond, the second electron is transferred. In contrast, in the EAS reaction coordinate where the aromatic ring is allowed to freely rotate (Figure 13), the ∠CCO becomes >163° and a two electron attack is observed as found for **O** in $[(DBED)_2Cu_2(O_2)]^{2+}$.[25]

Thus, both the **P** and **O** species are capable of performing aromatic hydroxylation via their separate mechanisms. The question now in tyrosinase and NspF is whether **P** is the reactive species or converts to **O** upon phenolic substrate

binding. The strength of the substrate−Cu interaction in the enzyme will be a key determining factor. While no substrate-bound oxy-CBC intermediate has been characterized spectroscopically, inhibitor binding studies have shown that substrate analogues bind to the Cu(II) in tyrosinase.[92,93] These studies also show that the interaction of the substrate with the protein pocket influences this binding. Thus, the combined influence of the Cu and protein pocket interactions will determine the nature of the Cu_2O_2 species; the stronger and more equatorial the substrate binding, the more favorable the conversion of **P** to **O**. These combined interactions will also determine the orientation of the substrate and whether the transfer of the electron pair is concerted during this electrophilic reaction.

■ ASSOCIATED CONTENT

ⓈSupporting Information

Cu K-edge XAS spectra of **1** and **2**; details of the DFT-optimized geometric and electronic structures of **1** and **2**; key geometries and electronic structures along the reaction coordinates for $[Cu(II)_2(NO_2\text{-}XYL)(O_2)]^{2+}$ (structures **A−L**) and $[Cu(II)_2(NH_3)_4(O_2)]^{2+}$ (structures **X−Z**); full *Gaussian 09* reference. This material is available free of charge via the Internet at http://pubs.acs.org.

■ AUTHOR INFORMATION

Corresponding Authors
hodgson@slac.stanford.edu
hedman@slac.stanford.edu
Edward.Solomon@stanford.edu

Notes
The authors declare no competing financial interest.

■ ACKNOWLEDGMENTS

■ REFERENCES

(1) Solomon, E. I.; Chen, P.; Metz, M.; Lee, S.-K.; Palmer, A. E. *Angew. Chem., Int. Ed.* **2001**, *40*, 4570−4590.
(2) Solomon, E. I.; Baldwin, M. J.; Lowery, M. D. *Chem. Rev.* **1992**, *92*, 521−542.
(3) Solomon, E. I.; Sundaram, U. M.; Machonkin, T. E. *Chem. Rev.* **1996**, *96*, 2563−2606.
(4) Mirica, L. M.; Ottenwaelder, X.; Stack, T. D. P. *Chem. Rev.* **2004**, *104*, 1013−1045.
(5) Lewis, E. A.; Tolman, W. B. *Chem. Rev.* **2004**, *104*, 1047−1076.
(6) Fukuzumi, S.; Karlin, K. D. *Coord. Chem. Rev.* **2013**, *257*, 187−195.
(7) Ginsbach, J. W.; Kieber-Emmons, M. T.; Nomoto, R.; Noguchi, A.; Ohnishi, Y.; Solomon, E. I. *Proc. Natl. Acad. Sci. U.S.A.* **2012**, *109*, 10793−10797.
(8) Hatcher, L. Q.; Karlin, K. D. *J. Biol. Inorg. Chem.* **2004**, *9*, 669−683.
(9) Jacobson, R. R.; Tyeklár, Z.; Farooq, A.; Karlin, K. D.; Liu, S.; Zubieta, J. *J. Am. Chem. Soc.* **1988**, *110*, 3690−3692.
(10) Baldwin, M. J.; Ross, P. K.; Pate, J. E.; Tyeklár, Z.; Karlin, K. D.; Solomon, E. I. *J. Am. Chem. Soc.* **1991**, *113*, 8671−8679.
(11) Schatz, M.; Becker, M.; Thaler, F.; Hampel, F.; Schindler, S.; Jacobson, R. R.; Tyeklár, Z.; Murthy, N. N.; Ghosh, P.; Chen, Q.; Zubieta, J.; Karlin, K. D. *Inorg. Chem.* **2001**, *40*, 2312−2322.
(12) Zhang, C. X.; Kaderli, S.; Costas, M.; Kim, E.-I.; Neuhold, Y.-M.; Karlin, K. D.; Zuberbühler, A. D. *Inorg. Chem.* **2003**, *42*, 1807−1824.
(13) A third end-on peroxo $Cu(II)_2$ species has also been observed.
(14) Comba, P. *Coord. Chem. Rev.* **2000**, *200−202*, 217−245.
(15) Park, G. Y.; Qayyum, M. F.; Woertink, J.; Hodgson, K. O.; Hedman, B.; Narducci Sarjeant, A. A.; Solomon, E. I.; Karlin, K. D. *J. Am. Chem. Soc.* **2012**, *134*, 8513−8524.
(16) Que, L.; Tolman, W. B. *Angew. Chem., Int. Ed.* **2002**, *41*, 1114−1137.
(17) Kitajima, N.; Fujisawa, K.; Moro-oka, Y.; Toriumi, K. *J. Am. Chem. Soc.* **1989**, *111*, 8975−8976.
(18) Kitajima, N.; Fujisawa, K.; Fujimoto, C.; Moro-oka, Y.; Hashimoto, S.; Kitagawa, T.; Toriumi, K.; Tatsumi, K.; Nakamura, A. *J. Am. Chem. Soc.* **1992**, *114*, 1277−1291.
(19) Magnus, K. A.; Hazes, B.; Ton-That, H.; Bonaventura, C.; Bonaventura, J.; Hol, W. G. *Proteins* **1994**, *19*, 302−309.
(20) Matoba, Y.; Kumagai, T.; Yamamoto, A.; Yoshitsu, H.; Sugiyama, M. *J. Biol. Chem.* **2006**, *281*, 8981−8990.
(21) Halfen, J. A.; Mahapatra, S.; Wilkinson, E. C.; Kaderli, S.; Young, V. G.; Que, L.; Zuberbühler, A. D.; Tolman, W. B. *Science* **1996**, *271*, 1397−1400.
(22) Mahapatra, S.; Halfen, J. A.; Wilkinson, E. C.; Pan, G.; Wang, X.; Young, V. G.; Cramer, C. J.; Que, L. J.; Tolman, W. B. *J. Am. Chem. Soc.* **1996**, *118*, 11555−11574.
(23) Mahadevan, V.; Hou, Z.; Cole, A. P.; Root, D. E.; Lal, T. K.; Solomon, E. I.; Stack, T. *J. Am. Chem. Soc.* **1997**, *119*, 11996−11997.
(24) Mirica, L. M.; Vance, M.; Rudd, D. J.; Hedman, B.; Hodgson, K. O.; Solomon, E. I.; Stack, T. D. P. *Science* **2005**, *308*, 1890−1892.
(25) Op't Holt, B. T.; Vance, M. A.; Mirica, L. M.; Heppner, D. E.; Stack, T. D. P.; Solomon, E. I. *J. Am. Chem. Soc.* **2009**, *131*, 6421−6438.
(26) Nasir, M. S.; Cohen, B. I.; Karlin, K. D. *J. Am. Chem. Soc.* **1992**, *114*, 2482−2494.
(27) Karlin, K. D.; Nasir, M. S.; Cohen, B. I.; Cruse, R. W.; Kaderli, S.; Zuberbühler, A. D. *J. Am. Chem. Soc.* **1994**, *116*, 1324−1336.
(28) Pidcock, E.; Obias, H. V.; Zhang, C. X.; Karlin, K. D.; Solomon, E. I. *J. Am. Chem. Soc.* **1998**, *120*, 7841−7847.
(29) Lam, B. M.; Halfen, J. A.; Young, V. G.; Hagadorn, J. R.; Holland, P. L.; Lledós, A.; Cucurull-Sánchez, L.; Novoa, J. J.; Alvarez, S.; Tolman, W. B. *Inorg. Chem.* **2000**, *39*, 4059−4072.
(30) DuBois, J. L.; Mukherjee, P.; Collier, A. M.; Mayer, J. M.; Solomon, E. I.; Hedman, B.; Stack, T. D. P.; Hodgson, K. O. *J. Am. Chem. Soc.* **1997**, *119*, 8578−8579.
(31) Szilagyi, R. K.; Metz, M.; Solomon, E. I. *J. Phys. Chem. A* **2002**, *106*, 2994−3007.
(32) Atanasov, M.; Comba, P.; Martin, B.; Müller, V.; Rajaraman, G.; Rohwer, H.; Wunderlich, S. *J. Comput. Chem.* **2006**, *27*, 1263−1277.
(33) This discussion of HF mixing needed in DFT calculations will be discussed further in another report.
(34) Cruse, R. W.; Kaderli, S.; Karlin, K. D. *J. Am. Chem. Soc.* **1988**, *110*, 6882−6883.
(35) Blackburn, N. J.; Strange, R. W.; Farooq, A.; Haka, M. S.; Karlin, K. D. *J. Am. Chem. Soc.* **1988**, *110*, 4263−4272.
(36) Cole, A. P.; Mahadevan, V.; Mirica, L. M.; Ottenwaelder, X.; Stack, T. *Inorg. Chem.* **2005**, *44*, 7345−7364.
(37) Tenderholt, A. L.; Hedman, B.; Hodgson, K. O. *PySpline*; Stanford Synchrotron Radiation Laboratory: Stanford, CA, 2006.
(38) Tenderholt, A.; Hedman, B.; Hodgson, K. O. *AIP Conf. Proc.* **2006**, *882*, 105−107.

(39) Frisch, M. J.; et al. *Gaussian 09 Revision A.1*; Gaussian, Inc.: Wallingford, CT, 2009.

(40) Neese, F. *ORCA: An ab Initio, DFT, and Semiempirical Electronic Structure Package, Version 2.6 Revision 35*; Universität Bonn: Bonn, Germany, 2008.

(41) Becke, A. D. *Phys. Rev. A* **1988**, *83*, 3098−3100.

(42) Perdew, J. *Phys. Rev. B* **1986**, *33*, 8822−8824.

(43) Lee, C.; Yang, W.; Parr, R. G. *Phys. Rev. B* **1988**, *37*, 785−789.

(44) Miehlich, B.; Savin, A.; Stoll, H.; Preuss, H. *Chem. Phys. Lett.* **1989**, *157*, 200−206.

(45) BLYP gives very similar results as BP86.

(46) Becke, A. D. *J. Chem. Phys.* **1993**, *98*, 5648−5652.

(47) Karlin, K. D.; Hayes, J. C.; Gultneh, Y.; Cruse, R. W.; McKown, J. W.; Hutchinson, J. P.; Zubieta, J. *J. Am. Chem. Soc.* **1984**, *106*, 2121−2128.

(48) Merrick, J. P.; Moran, D.; Radom, L. *J. Phys. Chem. A* **2007**, *111*, 11683−11700.

(49) http://cccbdb.nist.gov/vibscalejust.asp.

(50) Tomasi, J.; Mennucci, B.; Cammi, R. *Chem. Rev.* **2005**, *105*, 2999−3094.

(51) Grimme, S.; Antony, J.; Ehrlich, S.; Krieg, H. *J. Chem. Phys.* **2010**, *132*, 154104−154119.

(52) Jansen, G.; Hess, B. A. *Phys. Rev. A* **2011**, *39*, 6016−6017.

(53) Tenderholt, A. L. *QMForge, v. 2.1*; Stanford University: Stanford, CA, 2007; http://qmforge.sourceforge.net.

(54) Mulliken, R. *J. Chem. Phys.* **1955**, *23*, 1833−1840.

(55) Mayer, I. *Chem. Phys. Lett.* **1983**, *97*, 270−274.

(56) Bridgeman, A. J.; Cavigliasso, G.; Ireland, L. R.; Rothery, J. *J. Chem. Soc., Dalton Trans.* **2001**, 2095−2108.

(57) Humphrey, W.; Dalke, A.; Schulten, K. *J. Mol. Graphics* **1996**, *14*, 33−38.

(58) Yamaguchi, K.; Jensen, F.; Dorigo, A.; Houk, K. N. *Chem. Phys. Lett.* **1988**, *149*, 537−542.

(59) Kitagawa, Y.; Saito, T.; Ito, M.; Nakanishi, Y.; Shoji, M.; Koizumi, K.; Yamanaka, S.; Kawakami, T.; Okumura, M.; Yamaguchi, K. *Int. J. Quantum Chem.* **2007**, *107*, 3094−3102.

(60) For example, the BS spin expectation value for species **A** (C−O = 2.80 Å) is 0.87 (Table 7) with contamination from only the $S_T = 1$ excited state. Thus, eq 1 is used for energy correction. At the TS, the BS spin expectation value is 1.10 (Table 7) with spin contamination from the $S_T = 1$ and $S_T = 2$ excited states. An average spin expectation of 0.83 (average of the spin expectation values from species **A** to **F**, Supporting Information Table S11) was used as the spin contamination from the $S_T = 1$ state at the TS with the rest from the $S_T = 2$ state.

(61) de Groot, F. M. F. *Physica B* **1995**, *208−209*, 15−18.

(62) Fuggle, J. C.; Alvarado, S. F. *Phys. Rev. A* **1980**, *22*, 1615−1624.

(63) George, S. J.; Lowery, M. D.; Solomon, E. I.; Cramer, S. P. *J. Am. Chem. Soc.* **1993**, *115*, 2968−2969.

(64) Sarangi, R.; Aboelella, N.; Fujisawa, K.; Tolman, W. B.; Hedman, B.; Hodgson, K. O.; Solomon, E. I. *J. Am. Chem. Soc.* **2006**, *128*, 8286−8296.

(65) DeBeer George, S.; Metz, M.; Szilagyi, R. K.; Wang, H.; Cramer, S. P.; Lu, Y.; Tolman, W. B.; Hedman, B.; Hodgson, K. O.; Solomon, E. I. *J. Am. Chem. Soc.* **2001**, *123*, 5757−5767.

(66) High covalency can lead to shakeup satellite features on the L-edge which redistribute the intensity (*vide infra*), and therefore, total integrated intensities for **1** and **2** were used for comparison to square planar [CuCl₄]²⁻.

(67) Solomon, E. I.; Szilagyi, R. K.; DeBeer George, S.; Basumallick, L. *Chem. Rev.* **2004**, *104*, 419−458.

(68) Chen, P.; Root, D. E.; Campochiaro, C.; Fujisawa, K.; Solomon, E. I. *J. Am. Chem. Soc.* **2003**, *125*, 466−474.

(69) Mizuno, M.; Hayashi, H.; Fujinami, S.; Furutachi, H.; Nagatomo, S.; Otake, S.; Uozumi, K.; Suzuki, M.; Kitagawa, T. *Inorg. Chem.* **2003**, *42*, 8534−8544.

(70) Aboelella, N. W.; Lewis, E. A.; Reynolds, A. M.; Brennessel, W. W.; Cramer, C. J.; Tolman, W. B. *J. Am. Chem. Soc.* **2002**, *124*, 10660−10661.

(71) Hayashi, H.; Fujinami, S.; Nagatomo, S.; Ogo, S.; Suzuki, M.; Uehara, A.; Watanabe, Y.; Kitagawa, T. *J. Am. Chem. Soc.* **2000**, *122*, 2124−2125.

(72) Mahapatra, S.; Young, V. G.; Kaderli, S.; Zuberbühler, A. D.; Tolman, W. B. *Angew. Chem., Int. Ed.* **1997**, *36*, 130−133.

(73) Straub, B. F.; Rominger, F.; Hofmann, P. *Chem. Commun.* **2000**, 1611−1612.

(74) Zhou, L.; Powell, D.; Nicholas, K. M. *Inorg. Chem.* **2006**, *45*, 3840−3842.

(75) Henson, M. J.; Mukherjee, P.; Root, D. E.; Stack, T. D. P.; Solomon, E. I. *J. Am. Chem. Soc.* **1999**, *121*, 10332−10345.

(76) DFT calculations with B3LYP and the all-electron TZVP/SVP basis set generally overestimate the O−O stretching frequency in side-on peroxo Cu(II)₂ species by ∼100 cm⁻¹. In the **P**^NO₂−XYL complex, the frequency is overestimated by 132 cm⁻¹. This likely reflects an overestimation of the bend of the Cu₂O₂ dihedral angle, which has previously been shown in ref 77 to increase the O-O stretching frequency.

(77) Pidcock, E.; Obias, H. V.; Abe, M.; Liang, H.-C.; Karlin, K. D.; Solomon, E. I. *J. Am. Chem. Soc.* **1999**, *121*, 1299−1308.

(78) On the basis of the available crystal structure of [Cu(II)₂(H-XYL-O⁻)(OH⁻)]²⁺.

(79) Siegbahn, P. E. M.; Blomberg, M. R. A.; Chen, S.-L. *J. Chem. Theory Comput.* **2010**, *6*, 2040−2044.

(80) The reaction coordinates obtained with and without dispersion and relativistic effects are similar. The electronic structures of **1** and **2** also do not change significantly when dispersion and relativistic effects are added.

(81) Karlin, K. D.; Kaderli, S.; Zuberbühler, A. D. *Acc. Chem. Res.* **1997**, *30*, 139−147.

(82) The calculated DE‡ with 10% HF added, instead of 20% HF, is 23 kcal/mol, which is reduced to 13 kcal/mol when dispersion and relativistic effects are included.

(83) NIH shift experimentally observed with a methyl substituted at the C12 position (Figure 7) is calculated to take place after the TS and therefore does not affect the TS.

(84) The C−O MBO values in a fully optimized molecule of NO₂-phenolate and NO₂-phenol (without any Cu) are 1.807 and 1.233, respectively.

(85) There is a slight increase in charge and spin on the Cu centers that is due to approximately 11% α and β electron donation (2% α, 9% β from Cu₁ and 9% α, 3% β from Cu₂) from the coppers to the peroxo moiety (Table 8).

(86) At point **G** the peroxo π^* and σ^* orbitals are hybridized (Supporting Information Figure S2, orbitals 197 and 198). The peroxo σ^* (orbital 210 in Supporting Information Figure S2, **A**) is lowered in energy relative to the peroxo π_σ^* (LUMO, 197) at point **G**. For a planar Cu₂O₂ core, the peroxo π_σ^* HOMO is in the plane and is antibonding to Cu, whereas the π_v^* is out of the Cu₂O₂ plane and nonbonding to Cu. In the xylyl system, the peroxo π_σ^* and π_v^* orbitals hybridize because the Cu₂O₂ core is butterflied.

(87) The diradical formation is due to the peroxo π^* and σ orbitals hybridizing to maximize overlap with the π cloud of the substrate HOMO and resulting in greater overlap with the peroxo β LUMO compared to the peroxo a LUMO (Supporting Information Figure S3, point **Y**).

(88) Similar results are obtained with a five coordinate Cu system, [Cu(II)₂(NH₃)₆(O₂²⁻)]²⁺, instead of a four coordinate Cu species and with NO₂ substituted at the para position of the benzene.

(89) At the TS (Supporting Information Table S15, point **Y**), the Mülliken spins on the Cu centers decrease. However, the Mülliken charges (Supporting Information Table S14) also decrease showing that the Cu centers are not oxidized to Cu(III)'s.

(90) Synthetic modifications designed to experimentally probe for or induce radical intermediates, along with computational studies, are planned for future investigations.

(91) Similar results are obtained with water as the exogenous base.

(92) Winkler, M. E.; Lerch, K.; Solomon, E. I. *J. Am. Chem. Soc.* **1981**, *103*, 7001−7003.

(93) Wilcox, D. E.; Porras, A. G.; Hwang, Y. T.; Lerch, K.; Winkler, M. E.; Solomon, E. I. *J. Am. Chem. Soc.* **1985**, *107*, 4015−4027.

17431

dx.doi.org/10.1021/ja4078717 | *J. Am. Chem. Soc.* 2013, 135, 17417−17431